

KEK Preprint 2008-33

October 2008

A/H

A 160–320 GeV linear collider
to study

$e^+e^- \rightarrow HZ$ and $\gamma\gamma \rightarrow H, HH$

R. BELUSEVIC

IPNS, *High Energy Accelerator Research Organization* (KEK)

1-1 *Oho, Tsukuba, Ibaraki 305-0801, Japan*

belusev@post.kek.jp

“The changing of bodies into light, and light into bodies, is very conformable to the course of nature, which seems delighted with transmutations.”

Isaac Newton

Contents

1	Standard Model and Higgs mechanism	4
2	Higgs self-couplings	6
3	Single Higgs production in $\gamma\gamma$ collisions	7
4	Single Higgs production in e^+e^- annihilations	9
5	Higgs-pair production in $\gamma\gamma$ and e^+e^- collisions	10
6	Higgs couplings to SM particles	13
7	The proposed facility	15
8	Photon collider	16
9	X-band accelerator complex	17
10	Laser system for an X-band machine	18
11	Interaction region and beam dump	19
12	L-band (TESLA-type) accelerator complex	21
13	Laser system for an L-band machine	22
14	Luminosity and backgrounds at a $\gamma\gamma$ collider	23
15	Summary and Acknowledgements	25

References

Abstract: The construction of two electron linacs and an optical FEL system is proposed. This facility, which would serve primarily as a Higgs-boson collider factory, could be built in two stages, each with distinct physics objectives requiring particular center-of-mass (CM) energies: (1) $e^+e^- \rightarrow HZ$ ($E_{e^+e^-} \sim 250$ GeV), and (2) $\gamma\gamma \rightarrow H, HH$ ($E_{e^+e^-} \sim 160$ to 320 GeV). The rich set of final states in e^+e^- and $\gamma\gamma$ collisions would play an essential role in measuring the mass, spin, parity, two-photon width and trilinear self-coupling of the Higgs boson, as well as its couplings to fermions and gauge bosons; these quantities are difficult to determine with only one initial state. All the measurements made at LEP and SLC could be repeated using highly polarized electron beams and at much higher luminosities. For some processes within and beyond the Standard Model, the required CM energy is considerably lower at the proposed facility than at an e^+e^- or proton collider.

1 Standard Model and Higgs mechanism

Enormous progress has been made in the field of high-energy physics over the past four decades. The existence of a subnuclear world of quarks and leptons, whose dynamics can be described by quantum field theories possessing gauge symmetry (*gauge theories*), has been firmly established. The **Standard Model** (SM) of particle physics gives a coherent quantum-mechanical description of electromagnetic, weak and strong interactions based on fundamental constituents — quarks and leptons — interacting via force carriers — photons, W and Z bosons, and gluons.

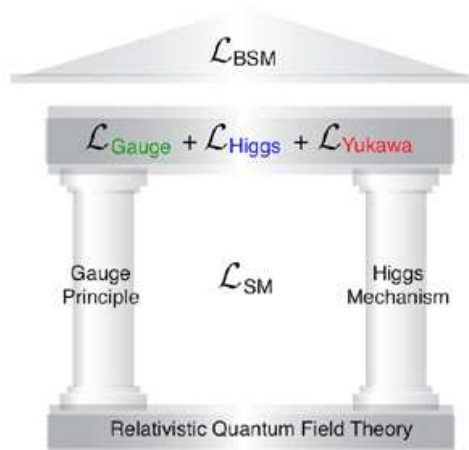


Figure 1: Two main pillars of the Standard Model (SM). The ‘BSM roof’ represents physics beyond the Standard Model. Reproduced courtesy of K. Fujii.

The Standard Model is supported by two theoretical ‘pillars’: the **gauge principle** and the **Higgs mechanism** for particle mass generation (see Fig. 1). Whereas the former has been established through precision electroweak measurements, the latter is essentially untested.

In the SM, where electroweak symmetry is broken by the Higgs mechanism, the mass of a particle depends on its interaction with the Higgs field, a medium that permeates the universe. The photon and gluon do not have such couplings, and so they remain massless. The Standard Model predicts the existence of a neutral spin-0 particle associated with the Higgs field, but it does not predict its mass. Although the existence of a Higgs field provides a simple mechanism for electroweak symmetry breaking, *our inability to predict the mass of the Higgs boson reflects the fact that we really do not understand at a fundamental level why this phenomenon occurs.*

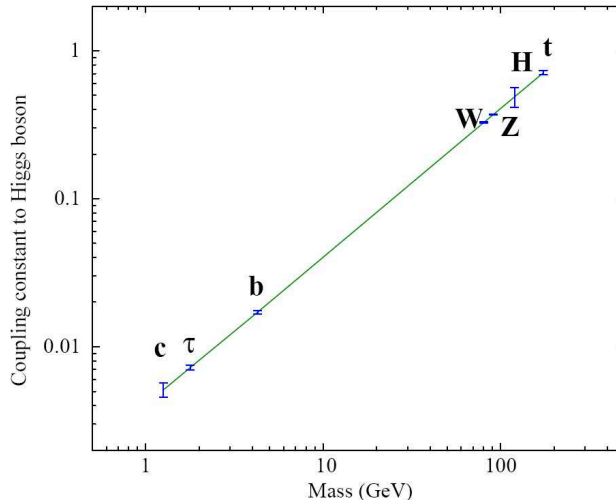


Figure 2: Precision with which the couplings of the Higgs particle with $m_H = 120$ GeV can be determined at an e^+e^- collider with $\int L = 500 \text{ fb}^{-1}$. The coupling κ_i of the particle i with mass m_i is defined so that the relation $m_i = v\kappa_i$ with $v \simeq 246$ GeV holds in the SM [1].

Another undesirable feature of the Standard Model is the *ad hoc* way in which fermion masses are introduced.

All of the couplings of the Higgs particle to gauge bosons and fermions are completely determined in the Standard Model in terms of electroweak coupling constants and fermion masses. Higgs production and decay processes can be computed in the SM unambiguously in terms of the Higgs mass alone. Since the coupling of the Higgs boson to fermions and gauge bosons is proportional to the particle masses (see Fig. 2), the Higgs boson will be produced in association with heavy particles and will decay into the heaviest particles that are kinematically accessible.

The rich set of final states in e^+e^- and $\gamma\gamma$ collisions would play an essential role in measuring the mass (m_H), spin, parity, two-photon width and trilinear self-coupling of the Higgs boson, as well as its couplings to fermions and gauge bosons; these quantities are difficult to determine with only one initial state.

The Higgs-boson mass affects the values of electroweak observables through radiative corrections. The precision electroweak data obtained over the past two decades consists of over a thousand individual measurements. Many of those measurements may be combined to provide a global test of consistency with the SM. The best constraint on m_H is obtained by making a global fit to the electroweak data. Such a fit strongly suggests that the most likely mass for the SM Higgs boson is just above the limit of 114.4 GeV set by direct searches at the LEP e^+e^- collider [2].

The dashed ellipse in Fig. 3 indicates the direct measurement of the W mass, m_W , and the top-quark mass, m_t . The elongated ellipse represents the predicted relationship between the two masses. Also shown is the correlation between m_W and m_t as expected in the Standard Model for different values of the Higgs-boson mass m_H (the diagonal band). Notice that the two ellipses overlap near the lines of constant m_H . This indicates that the Standard Model is a fairly good approximation to reality. Both ellipses are consistent with a low value of the Higgs-boson mass.

High-precision electroweak measurements, therefore, provide a natural complement to direct studies of the Higgs sector. All the measurements made at LEP and SLC could be repeated at the proposed facility using 90% polarized electron beams and at much higher luminosities. Assuming a geometric luminosity $L_{e^+e^-} \approx 5 \times 10^{33} \text{ cm}^{-2} \text{ s}^{-1}$ at the Z resonance, about 2×10^9 Z bosons can be produced in an operational year of 10^7 s. This is about 200 times the entire LEP statistics. Moreover, about 10^6 W bosons can be produced near the W-pair threshold at the optimal energy point for measuring the W-boson mass. An increase in the number of Z events by two orders of magnitude as compared to LEP data, and a substantially improved accuracy in the measurement of W-boson properties, would provide new opportunities for high-precision electroweak studies [3].

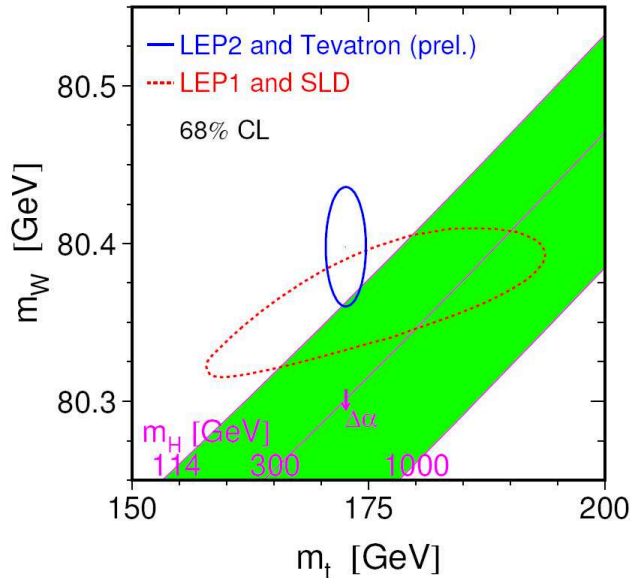


Figure 3: Direct and indirect constraints on the W and top-quark masses. Reprinted courtesy of LEP Electroweak Working Group (March 2008).

2 Higgs self-couplings

In order to provide a mechanism for the generation of particle masses in the **Standard Model** without violating its gauge invariance, a complex scalar SU(2) doublet Φ with four real fields and *hypercharge* $Y = 1$ is introduced. The dynamics of the field Φ is described by the Lagrangian

$$\mathcal{L}_\Phi = (D_\mu \Phi)^\dagger (D^\mu \Phi) - \mu^2 \Phi^\dagger \Phi - \lambda (\Phi^\dagger \Phi)^2 \quad (1)$$

where $(D_\mu \Phi)^\dagger (D^\mu \Phi)$ is the kinetic-energy term and $\mu^2 \Phi^\dagger \Phi + \lambda (\Phi^\dagger \Phi)^2$ is the Higgs self-interaction potential. In the so-called *unitary gauge*,

$$\Phi = \frac{1}{\sqrt{2}} \begin{pmatrix} 0 \\ v + H \end{pmatrix} \quad (2)$$

where $v \equiv \sqrt{-\mu^2/\lambda} = 246$ GeV is the **vacuum expectation value** of the scalar field Φ . The Higgs self-interaction potential gives rise to terms involving only the physical **Higgs field** H:

$$V_H = \frac{1}{2} (2\lambda v^2) H^2 + \lambda v H^3 + \frac{\lambda}{4} H^4 \quad (3)$$

We see from Eq. (3) that the **Higgs mass** $m_H = \sqrt{2\lambda} v$ is related to the quadrilinear self-coupling strength λ . It is also evident that the **trilinear self-coupling** of the Higgs field is

$$\lambda_{\text{HHH}} \equiv \lambda v = \frac{m_H^2}{2v} \quad (4)$$

and the self-coupling among four Higgs fields

$$\lambda_{\text{HHHH}} \equiv \frac{\lambda}{4} = \frac{m_H^2}{8v^2} \quad (5)$$

Note that the Higgs self-couplings are uniquely determined by the mass of the Higgs boson, which represents a free parameter of the model.

Any theoretical model based on the gauge principle must evoke spontaneous symmetry breaking. For example, the minimal *supersymmetric* extension of the Standard Model (**MSSM**) introduces two SU(2) doublets of complex Higgs fields, whose neutral components have vacuum expectation values v_1 and v_2 . In this model, spontaneous electroweak symmetry breaking results in five physical Higgs-boson states: two neutral scalar fields h^0 and H^0 , a pseudoscalar A^0 and two charged bosons H^\pm . This extended Higgs system can be described at tree level by two parameters: the ratio $\tan\beta \equiv v_2/v_1$, and a mass parameter, which is generally identified with the mass of the pseudoscalar boson A^0 , m_A . While there is a bound of about 140 GeV on the mass of the lightest CP-even neutral Higgs boson h^0 [4, 5], the masses of the H^0 , A^0 and H^\pm bosons may be much larger. The existence of the Higgs boson h^0 is the only verifiable low-energy prediction of the MSSM model.

The trilinear self-coupling of the lightest MSSM Higgs boson at tree level is given by

$$\lambda_{hhh} = \frac{m_Z^2}{2v} \cos 2\alpha \sin(\beta + \alpha) \quad (6)$$

where

$$\tan 2\alpha = \tan 2\beta \frac{m_A^2 + m_Z^2}{m_A^2 - m_Z^2} \quad (7)$$

We see that for arbitrary values of the MSSM input parameters $\tan\beta$ and m_A the value of the h^0 self-coupling differs from that of the SM Higgs boson. However, in the so-called ‘decoupling limit’ $m_A^2 \sim m_{H^0}^2 \sim m_{H^\pm}^2 \gg v^2/2$, the trilinear and quadrilinear self-couplings of the lightest CP-even neutral Higgs boson h^0 approach the SM value.

In contrast to any anomalous couplings of the gauge bosons, an anomalous self-coupling of the Higgs particle would contribute to electroweak observables only at two-loop and higher orders, and is therefore practically unconstrained by precision electroweak measurements [6].

3 Single Higgs production in $\gamma\gamma$ collisions

Since photons couple directly to all fundamental fields carrying the electromagnetic current (leptons, quarks, W bosons, supersymmetric particles), $\gamma\gamma$ collisions provide a comprehensive means of exploring virtually every aspect of the SM and its extensions (see [7], [8] and references therein). The production mechanisms in e^+e^- collisions are often more complex and model-dependent. Moreover, the cross-sections for production of charged-particle pairs in $\gamma\gamma$ interactions are approximately an order of magnitude larger than in e^+e^- annihilations.

In $\gamma\gamma$ collisions, the **Higgs boson** is produced as a single resonance in a state of definite CP, which is perhaps the most important advantage over e^+e^- annihilations, where this s -channel process is highly suppressed. For the Higgs mass in the range $m_H = 115\text{--}200$ GeV, the effective cross-section for $\gamma\gamma \rightarrow H$ is about a factor of five larger than that for Higgs production in e^+e^- annihilations. In this mass range, the process $e^+e^- \rightarrow HZ$ requires considerably higher center-of-mass energies than $\gamma\gamma \rightarrow H$. In e^+e^- annihilations, the heavy neutral MSSM Higgs bosons can be created only by associated production ($e^+e^- \rightarrow H^0 A^0$), whereas in $\gamma\gamma$ collisions they are produced as single resonances ($\gamma\gamma \rightarrow H^0, A^0$) with masses up to 80% of the initial e^+e^- collider energy [9].

Furthermore, calculations show that the *statistical* sensitivity of the cross-section $\sigma_{\gamma\gamma \rightarrow HH}$ to the **Higgs self-coupling** is maximal near the $2m_H$ threshold for m_H between 115 and 160 GeV, and is comparable with the statistical sensitivities of $\sigma_{e^+e^- \rightarrow HHZ}$ and $\sigma_{e^+e^- \rightarrow HH\nu\bar{\nu}}$ to this coupling for $E_{ee} \leq 700$ GeV [10]. The overall *acceptance* is expected to be considerably larger in $\gamma\gamma \rightarrow HH$ than in the process $e^+e^- \rightarrow HH\nu\bar{\nu}$. Note also that hadron colliders are not well suited for measuring the self-coupling of the Higgs boson if $m_H \leq 140$ GeV [11].

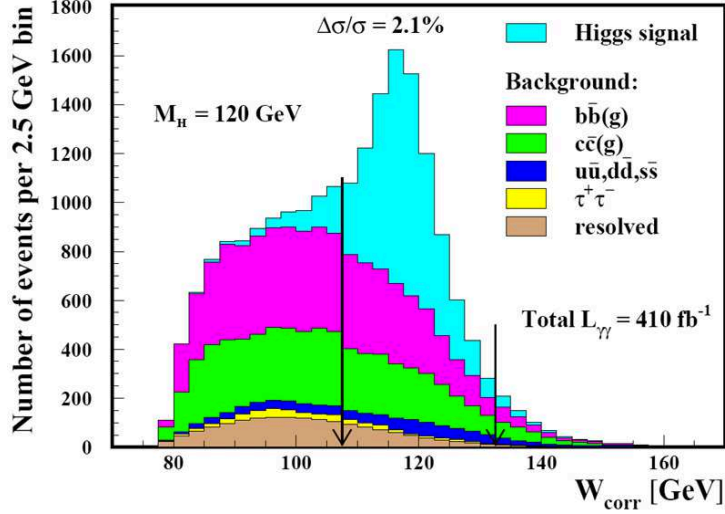


Figure 4: The reconstructed invariant-mass distribution of the $\gamma\gamma \rightarrow H \rightarrow b\bar{b}$ signal and the $b\bar{b}(g)$ and $c\bar{c}(g)$ backgrounds. The gluon (‘resolved’) structure of the photon can be measured *in situ*. Credit: P. Niezurawski, A. Zarnecki and M. Krawczyk.

The reaction $\gamma\gamma \rightarrow H$, which is related to $H \rightarrow \gamma\gamma$, proceeds through a ‘loop diagram’ and receives contributions from *all* charged particles that couple to the photon and the Higgs boson. Thus, the **two-photon width** $\Gamma(H \rightarrow \gamma\gamma)$ is sensitive to the Higgs-top Yukawa coupling, as well as mass scales far beyond the energy of the $\gamma\gamma$ collision. Assuming that the branching ratio $\text{BR}(H \rightarrow b\bar{b})$ can be measured to an accuracy of about 2% in the process $e^+e^- \rightarrow \text{HZ}$, the $\gamma\gamma$ partial width can be determined with a similar precision for $m_H \simeq 120$ GeV by measuring the cross-section $\sigma(\gamma\gamma \rightarrow H \rightarrow b\bar{b}) \propto \Gamma(H \rightarrow \gamma\gamma)\text{BR}(H \rightarrow b\bar{b})$. The Higgs-top coupling can also be measured in the process $e^+e^- \rightarrow t\bar{t}$ at the pair-production threshold [12].

Both the energy spectrum and polarization of the backscattered photons depend strongly on the polarizations of the incident electrons and laser photons. The key advantage of using e^-e^- beams is that they can be polarized to a high degree, enabling one to tailor the photon energy distribution to one’s needs. In a collision of two photons, the possible helicities are 0 or 2. For example, the Higgs boson is produced in the $J_z = 0$ state, whereas the background processes $\gamma\gamma \rightarrow b\bar{b}$, $c\bar{c}$ are suppressed for this helicity configuration (see Fig. 4). The circular polarization of the photon beams is therefore an important asset, for it can be used both to enhance the signal and suppress the background.

The **CP properties** of any neutral Higgs boson that may be produced at a photon collider can be *directly* determined by controlling the polarizations of Compton-scattered photons [13]. A CP-even Higgs boson couples to the combination $\mathbf{e}_1 \cdot \mathbf{e}_2$, whereas a CP-odd Higgs boson couples to $(\mathbf{e}_1 \times \mathbf{e}_2) \cdot \mathbf{k}_\gamma$:

$$\mathcal{M}(\gamma\gamma \rightarrow H[0^{++}]) \propto \mathbf{e}_1 \cdot \mathbf{e}_2 \propto 1 + \cos 2\phi$$

$$\mathcal{M}(\gamma\gamma \rightarrow A[0^{-+}]) \propto (\mathbf{e}_1 \times \mathbf{e}_2) \cdot \mathbf{k}_\gamma \propto 1 - \cos 2\phi$$

where \mathbf{e}_i are polarization vectors of colliding photons, ϕ is the angle between them, and \mathbf{k}_γ is the momentum vector of one of the Compton-scattered photons; 0^{++} and 0^{-+} are the quantum numbers J^{PC} . The scalar (pseudoscalar) Higgs boson couples to *linearly polarized* photons with a maximum strength if the polarization vectors are parallel (perpendicular): $\sigma \propto 1 \pm l_1 l_2 \cos 2\phi$, where l_i are the degrees of linear polarization; the signs \pm correspond to the $\text{CP} = \pm 1$ particles.

The general amplitude for a CP-*mixed state* to couple to the two photons is

$$\mathcal{M} = \mathcal{E}(\mathbf{e}_1 \cdot \mathbf{e}_2) + \mathcal{O}(\mathbf{e}_1 \times \mathbf{e}_2)_z \quad (8)$$

where \mathcal{E} is the CP-even and \mathcal{O} the CP-odd contribution to the amplitude. If we denote the *helicities* of the two photons by λ_1 and λ_2 , with $\lambda_1, \lambda_2 = \pm 1$, then the above vector products can be expressed as

$$\mathbf{e}_1 \cdot \mathbf{e}_2 = -(1 + \lambda_1 \lambda_2)/2 \quad (\mathbf{e}_1 \times \mathbf{e}_2)_z = i\lambda_1(1 + \lambda_1 \lambda_2)/2$$

Now, $|\mathcal{M}_{++}|^2 - |\mathcal{M}_{--}|^2 = -4\text{Im}(\mathcal{E}\mathcal{O}^*)$, $2\text{Re}(\mathcal{M}_{--}^* \mathcal{M}_{++}) = 2(|\mathcal{E}|^2 - |\mathcal{O}|^2)$ and $2\text{Im}(\mathcal{M}_{--}^* \mathcal{M}_{++}) = -4\text{Re}(\mathcal{E}\mathcal{O}^*)$. When these expressions are divided by $|\mathcal{M}_{++}|^2 + |\mathcal{M}_{--}|^2 = 2(|\mathcal{E}|^2 + |\mathcal{O}|^2)$, we obtain three polarization asymmetries that give an unambiguous measure of CP-mixing [13]. Note that these require both *linearly* and *circularly* polarized photons.

In e^+e^- annihilations, it is straightforward to discriminate between CP-even and CP-odd neutral Higgs bosons, but would be difficult to detect small CP-violating effects (which contribute only at the one-loop level) for a dominantly CP-even component (which contributes at the tree level in e^+e^- collisions) [14].

4 Single Higgs production in e^+e^- annihilations

A particularly noteworthy feature of an e^+e^- collider is that the Higgs boson can be detected in the **Higgs-strahlung process**

$$e^+e^- \rightarrow \text{HZ} \tag{9}$$

even if it decays into invisible particles (e.g., the lightest *neutralino* of a supersymmetric model). In this case the signal manifests itself as a peak in the distribution of invariant mass of the system recoiling against the lepton pair stemming from Z-boson decay (see Fig. 5).

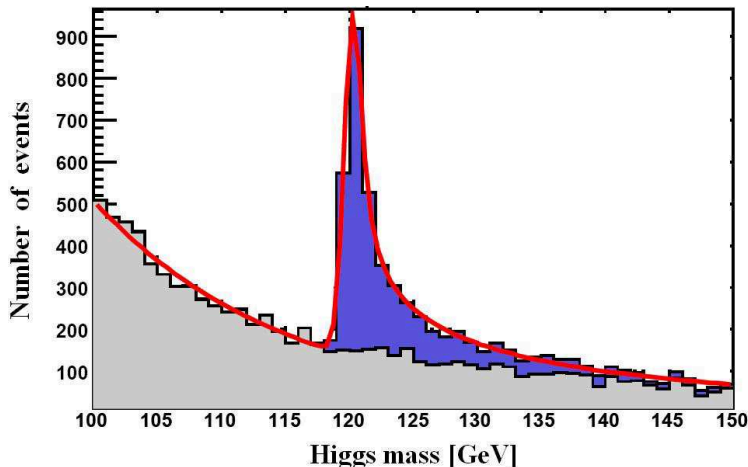


Figure 5: Distribution of the invariant mass of the system recoiling against a pair of leptons in the process $e^+e^- \rightarrow \text{HZ} \rightarrow X\ell^+\ell^-$ for $m_H = 120$ GeV and $\int \mathcal{L} = 500 \text{ fb}^{-1}$ at $\sqrt{s} = 250$ GeV. The red line is a fit to a Monte Carlo simulation of the Higgs signal and the ZZ background; the gray area represents the background only [15]. For $m_H \simeq 120$ GeV, the optimum center-of-mass energy is $\sqrt{s} \simeq 230$ GeV.

By exploiting the $\text{HZ} \rightarrow X\ell^+\ell^-$ channel, the Higgs-strahlung **cross-sections** can be measured with statistical errors of 2.6 to 3.1 percent for Higgs-boson masses from 120 to 160 GeV (see [16] and references therein).

From the fits to the reconstructed mass spectra in the channels $\text{HZ} \rightarrow q\bar{q}\ell^+\ell^-$, $b\bar{b}q\bar{q}$, $\text{WW}\ell^+\ell^-$ and $\text{WW}q\bar{q}$, the **Higgs-boson mass** can be determined with an uncertainty of 40 to 70 MeV for m_H in the range 120 to 180 GeV [16].

To determine the **spin** and **parity** of the SM Higgs boson in the Higgs-strahlung process, one can use the information on (1) the energy dependence of the Higgs-boson production cross-section just above the kinematic threshold, and (2) the angular distribution of the Z/H bosons. The best way to study the **CP properties** of the Higgs boson is by analyzing the spin correlation effects in the decay channel $H \rightarrow \tau^+ \tau^-$ (see [16] and references therein).

The Higgs-strahlung cross-section, which dominates at low CM energies, decreases with energy in proportion to $1/s$ (see Eq. (21)). In contrast, the cross-section for the **W-fusion process**

$$e^+ e^- \rightarrow H \nu_e \bar{\nu}_e \quad (10)$$

increases with energy in proportion to $\log(s/m_H^2)$, and hence becomes more important at energies $\sqrt{s} \gtrsim 500$ GeV for the Higgs-mass range $115 \text{ GeV} \lesssim m_H \lesssim 200 \text{ GeV}$.

5 Higgs-pair production in $\gamma\gamma$ and e^+e^- collisions

It is well known that hadron colliders are not ideally suited for measuring the self-coupling of the Higgs boson if $m_H \leq 140$ GeV [11]. The potential of a future $\gamma\gamma/e^+e^-$ collider for determining the HHH coupling has therefore been closely examined (see [10] and [17, 18, 19, 20]).

The production of a pair of SM Higgs bosons in photon-photon collisions,

$$\gamma\gamma \rightarrow HH \quad (11)$$

which is related to the Higgs-boson decay into two photons, is due to W-boson and top-quark box and triangle loop diagrams. The total cross-section for $\gamma\gamma \rightarrow HH$ in polarized photon-photon collisions, calculated at the leading one-loop order [21] as a function of the $\gamma\gamma$ center-of-mass energy and for m_H between 115 and 150 GeV, is shown in Fig. 6a. The cross-section calculated for equal photon helicities, $\sigma_{\gamma\gamma \rightarrow HH}(J_z = 0)$, rises sharply above the $2m_H$ threshold for different values of m_H , and has a peak value of about 0.4 fb at a $\gamma\gamma$ center-of-mass energy of 400 GeV. In contrast, the cross-section for opposite photon helicities, $\sigma_{\gamma\gamma \rightarrow HH}(J_z = 2)$, rises more slowly with energy because a pair of Higgs bosons is produced in a state with orbital angular momentum of at least $2\hbar$.

The cross-sections for equal photon helicities are of special interest, since only the $J_z = 0$ amplitudes contain contributions with trilinear Higgs self-coupling. By adding to the SM Higgs potential $V(\Phi^\dagger\Phi)$ a gauge-invariant dimension-6 operator $(\Phi^\dagger\Phi)^3$, one introduces a gauge-invariant anomalous trilinear Higgs coupling $\delta\kappa$ [21]. For the reaction $\gamma\gamma \rightarrow HH$, the only effect of such a coupling in the *unitary gauge* would be to replace the trilinear HHH coupling of the SM in Eq. 4 by an **anomalous Higgs self-coupling**

$$\lambda = (1 + \delta\kappa)\lambda_{\text{HHH}} \quad (12)$$

The dimensionless anomalous coupling $\delta\kappa$ is normalized so that $\delta\kappa = -1$ exactly cancels the SM HHH coupling. The cross-sections $\sigma_{\gamma\gamma \rightarrow HH}$ for five values of $\delta\kappa$ are shown in Fig. 6b.

In an experiment to measure the trilinear Higgs self-coupling, the contribution from $\gamma\gamma \rightarrow HH$ for opposite photon helicities represents an irreducible background. However, this background is suppressed if one chooses a $\gamma\gamma$ center-of-mass energy below about 320 GeV.

To ascertain the potential of $\gamma\gamma$ colliders for measuring an anomalous trilinear Higgs self-coupling, one must take into account the fact that the photons are not monochromatic [22]. It is envisaged that an e^-e^- linac and a terawatt laser system will be used to produce Compton-scattered γ -ray beams for a photon collider. Both the energy spectrum and polarization of the backscattered photons depend strongly on the polarizations of the incident electrons and photons. A longitudinal electron-beam polarization of 90% and a 100% circular polarization of laser photons are assumed throughout.

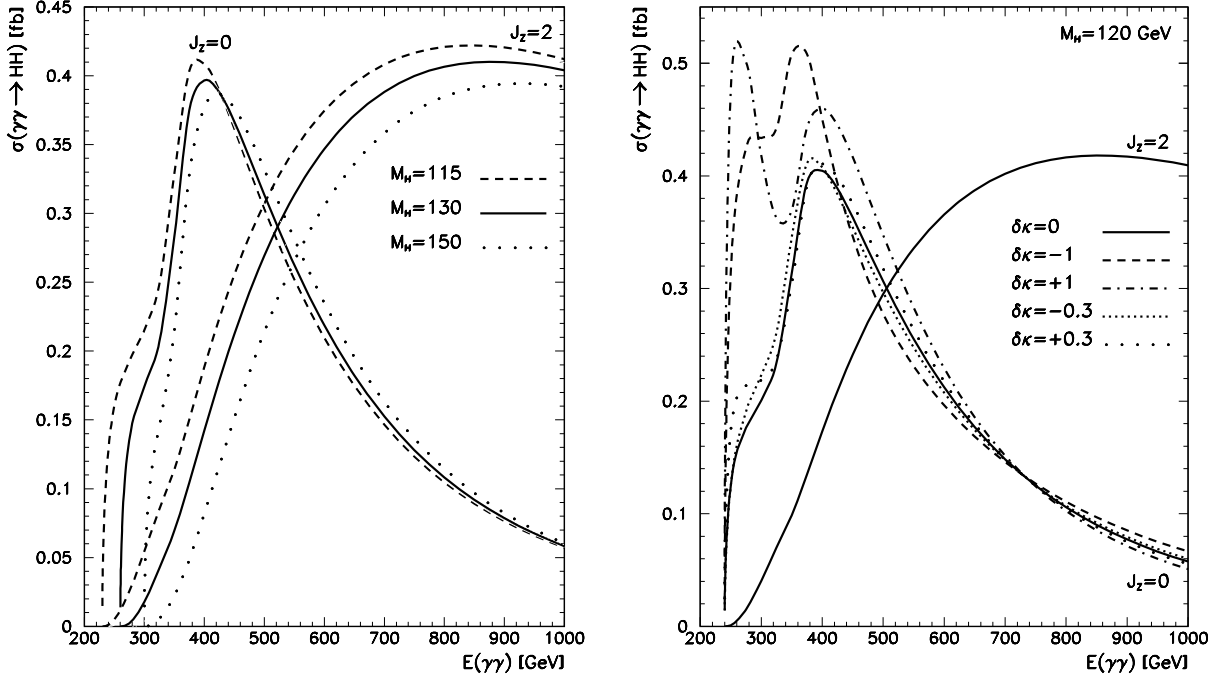


Figure 6: (a) The total $\gamma\gamma \rightarrow \text{HH}$ cross-section as a function of the $\gamma\gamma$ center-of-mass energy. Contributions for equal ($J_z = 0$) and opposite ($J_z = 2$) photon helicities are shown separately. (b) The cross-sections for HH production in $\gamma\gamma$ collisions for $m_{\text{H}} = 120$ GeV and anomalous trilinear Higgs self-couplings $\delta\kappa = 0, \pm 1, \pm 0.3$. Credit: R. Belusevic & G. Jikia [10].

The trilinear self-coupling of the Higgs boson can also be measured either in the so-called **double Higgs-strahlung process**

$$e^+e^- \rightarrow \text{HHZ} \quad (13)$$

or in the **W-fusion reaction**

$$e^+e^- \rightarrow \text{HH}\nu_e\bar{\nu}_e \quad (14)$$

The total cross-section for pair production of 120-GeV Higgs bosons in e^+e^- collisions, calculated for *unpolarized* beams, is presented in Fig. 7 for anomalous trilinear Higgs self-couplings $\delta\kappa = 0$ or -1 . If the electron beam is 100% polarized, the double Higgs-strahlung cross-section will stay approximately the same, while the W-fusion cross-section will be twice as large. From Fig. 7 we infer that the SM double Higgs-strahlung cross-section exceeds 0.1 fb at 400 GeV for $m_{\text{H}} = 120$ GeV, and reaches a broad maximum of about 0.2 fb at a CM energy of 550 GeV. The SM cross-section for W-fusion stays below 0.1 fb for CM energies up to 1 TeV.

For $m_{\text{H}} = 120$ GeV, and assuming a longitudinal electron-beam polarization of 90%, the maximum sensitivity to an anomalous trilinear Higgs self-coupling is achieved in the double Higgs-strahlung process at a CM energy of about 500 GeV [10]. This is significantly higher than the optimal CM energy in $\gamma\gamma$ collisions. In the W-fusion process, a similar sensitivity is attained at $E(e^+e^-) \approx 600$ GeV.

Calculations show that the *statistical* sensitivity of $\sigma_{\gamma\gamma \rightarrow \text{HH}}$ to the Higgs self-coupling is maximal near the kinematic threshold for Higgs-pair production for m_{H} between 115 and 150 GeV, and is comparable with the sensitivities of $\sigma_{e^+e^- \rightarrow \text{HHZ}}$ and $\sigma_{e^+e^- \rightarrow \text{HH}\nu\bar{\nu}}$ to this coupling for $E_{ee} \leq 700$ GeV, even if the integrated luminosity in $\gamma\gamma$ collisions is only one third of that in e^+e^- annihilations [10]. As mentioned earlier, the overall *acceptance* is expected to be considerably larger in the process $\gamma\gamma \rightarrow \text{HH}$ than in the reaction $e^+e^- \rightarrow \text{HH}\nu\bar{\nu}$.

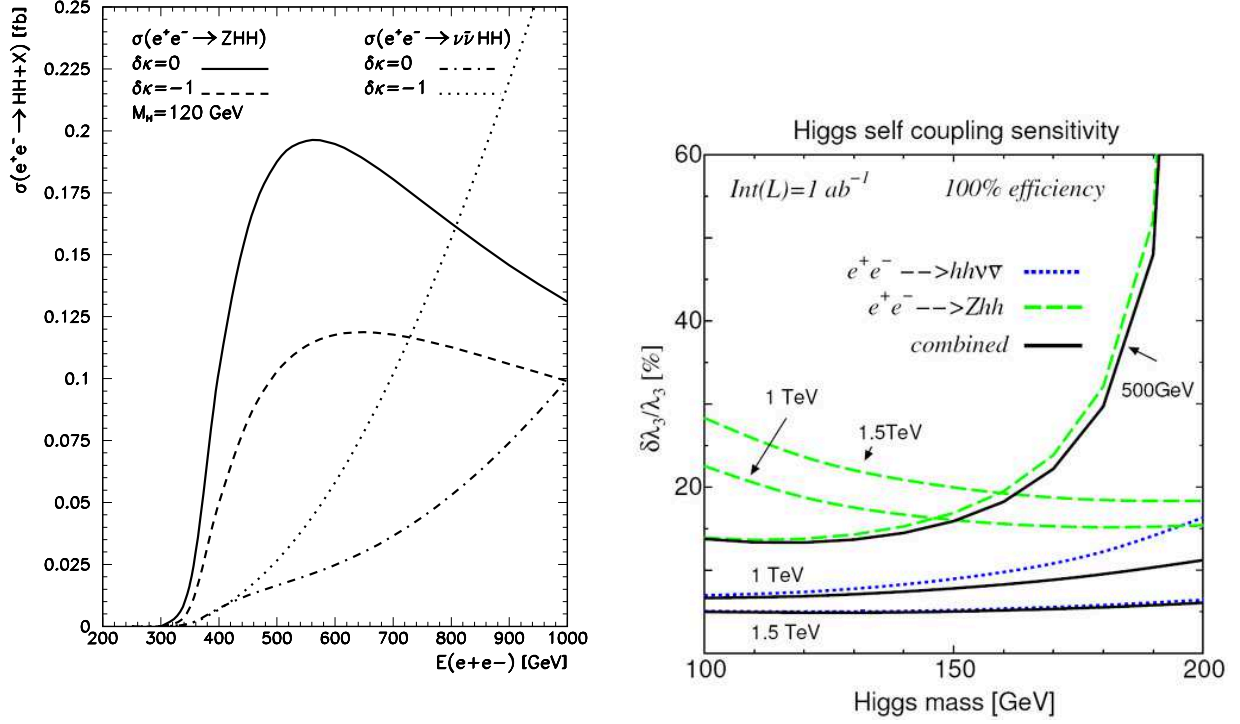


Figure 7: (a) Total cross-sections for $e^+e^- \rightarrow HHZ$ and $e^+e^- \rightarrow HH\nu_e\bar{\nu}_e$ as functions of the e^+e^- CM energy for $m_H = 120$ GeV and the anomalous trilinear Higgs self-couplings $\delta\kappa = 0$ or -1 ; Credit: R. Belusevic & G. Jikia [10]. (b) Statistical sensitivity of the trilinear self-coupling for the processes $e^+e^- \rightarrow HHZ$ and $e^+e^- \rightarrow HH\nu_e\bar{\nu}_e$ [1].

The Feynman diagrams for the process $\gamma\gamma \rightarrow HH$ are shown in Fig. 1 of [21]. New physics beyond the Standard Model introduces additional complexity into the subtle interplay between the Higgs ‘pole amplitudes’ and the top-quark and W-boson ‘box diagrams’:

$$|\mathcal{M}(J_z = 0)|^2 = |A(s)(\lambda_{\text{SM}} + \delta\lambda) + B|^2$$

where λ_{SM} is the trilinear Higgs self-coupling in the SM. From the above expression we infer that the cross-section for $\gamma\gamma \rightarrow HH$ is a quadratic function of $\lambda \equiv \lambda_{\text{SM}} + \delta\lambda$:

$$\sigma(\lambda) = \alpha\lambda^2 + \beta\lambda + \gamma \quad \alpha > 0, \quad \gamma > 0$$

There are various ways to define the sensitivity of the trilinear Higgs self-coupling. For instance, we can expand around $\sigma = \sigma_{\text{SM}}$, and express the number of events as

$$N = L\sigma_{\text{SM}} + L\delta\lambda\left(\frac{d\sigma}{d\lambda}\right)_{\lambda=\lambda_{\text{SM}}} + \dots$$

where L is the integrated luminosity. The sensitivity of λ is given by

$$\sqrt{N} = \left| L\delta\lambda\left(\frac{d\sigma}{d\lambda}\right)_{\lambda=\lambda_{\text{SM}}} \right|$$

i.e.,

$$\delta\lambda = \frac{\sqrt{L\sigma_{\text{SM}}}}{L(d\sigma/d\lambda)_{\lambda=\lambda_{\text{SM}}}} = \frac{\sqrt{\sigma_{\text{SM}}/L}}{(d\sigma/d\lambda)_{\lambda=\lambda_{\text{SM}}}}$$

A plot of the trilinear Higgs self-coupling sensitivity in $\gamma\gamma$ collisions, based on the above expression for $\delta\lambda$, is shown in Fig. 8; for e^+e^- annihilations, see Fig. 3.8 in [16]. An obvious

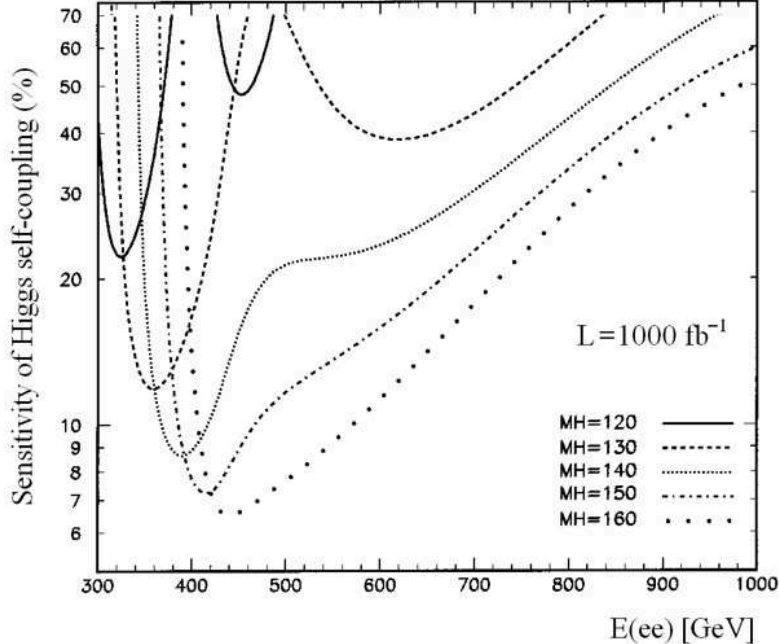


Figure 8: Statistical sensitivity of the trilinear Higgs self-coupling for various Higgs-boson masses assuming $\int \mathcal{L} = 1000 \text{ fb}^{-1}$. Based on the calculation by R. Belusevic & G. Jikia described in [10].

drawback of the above definition of $\delta\lambda$ is that its value becomes unphysically large when the derivative $d\sigma/d\lambda \rightarrow 0$, which means that one should take into account also the λ^2 term.

Since the cross-section $\sigma_{\gamma\gamma \rightarrow \text{HH}}$ does not exceed 0.4 fb , it is essential to attain the highest possible luminosity, rather than energy, in order to measure the trilinear Higgs self-coupling. As shown in [10], appropriate angular and invariant-mass cuts and a b -tagging requirement, which result in a Higgs-pair reconstruction efficiency of about 50%, would suppress the dominant W -pair and four-quark backgrounds well below the HH signal. For such a reconstruction efficiency, a center-of-mass energy $E_{ee} \approx 300 \text{ GeV}$ and $m_H = 120 \text{ GeV}$ an integrated $\gamma\gamma$ luminosity $L_{\gamma\gamma} \approx 450 \text{ fb}^{-1}$ would be needed to exclude a zero trilinear Higgs-boson self-coupling at the 5σ level (statistical uncertainty only). An even higher luminosity is required for an accurate measurement of this coupling.

6 Higgs couplings to SM particles

In the *unitary gauge*, the kinetic term in Eq. (1) can be expressed as

$$(D_\mu \Phi)^\dagger (D^\mu \Phi) = \frac{1}{2} (\partial_\mu \text{H})^2 + \frac{g^2}{4} (v + \text{H})^2 \left(W_\mu^+ W^{-\mu} + \frac{Z_\mu Z^\mu}{2 \cos^2 \theta_W} \right) \quad (15)$$

where $D_\mu \Phi$ is the *covariant derivative* of Φ and

$$\cos \theta_W = \frac{g}{\sqrt{g^2 + g'^2}} \quad g \sin \theta_W = g' \cos \theta_W = e \quad (16)$$

(g and g' are the electroweak couplings and e is the electric charge). A comparison with the usual mass terms for the charged and neutral vector bosons reveals that

$$m_W = \frac{gv}{2} \quad (17)$$

$$m_Z = \frac{gv}{2 \cos \theta_W} = \frac{m_W}{\cos \theta_W} \quad (18)$$

From Eq. (15) we also infer that the **Higgs-gauge boson couplings** are

$$\lambda_{\text{HWW}} \equiv \frac{g^2 v}{2} = \frac{2m_{\text{W}}^2}{v} \quad (19)$$

and

$$\lambda_{\text{HZZ}} \equiv \frac{g^2 v}{4 \cos^2 \theta_{\text{W}}} = \frac{m_{\text{Z}}^2}{v} \quad (20)$$

Therefore, the Higgs couplings to gauge bosons are proportional to their masses. This can be readily verified by measuring the production cross-sections in the Higgs-strahlung and W-fusion processes. At center-of-mass energies $s \gg m_{\text{H}}^2$,

$$\begin{aligned} \sigma(e^+ e^- \rightarrow \text{HZ}) &\propto \lambda_{\text{HZZ}}^2 / s \\ \sigma(e^+ e^- \rightarrow \text{H}\nu\bar{\nu}) &\propto \lambda_{\text{HWW}}^2 \log(s/m_{\text{H}}^2) \end{aligned} \quad (21)$$

The cross-section $\sigma(e^+ e^- \rightarrow \text{HZ}) \rightarrow \text{H}\ell^+ \ell^-$ can be measured independently of the Higgs-boson decay modes by analyzing the invariant mass of the system recoiling against the Z boson (see Section 4).

The vector bosons are coupled to the ground-state Higgs field by means of the covariant derivative (see Eq. (15)). The **Higgs-fermion couplings** are introduced in an *ad hoc* way through the *Yukawa Lagrangian*

$$\mathcal{L} = -g_f \bar{\psi}_f \psi_f \Phi \quad (22)$$

Replacing the Higgs field by its ground-state value, $\Phi \rightarrow v/\sqrt{2}$ (see Eq. (2)), yields the mass term $-m_f \bar{\psi}_f \psi_f$, where $m_f = g_f v/\sqrt{2}$. The interaction term in the Lagrangian is obtained by the replacement $\Phi \rightarrow \text{H}/\sqrt{2}$:

$$\mathcal{L}_{\text{int}} = -\frac{m_f}{v} \text{H} \bar{\psi}_f \psi_f \quad (23)$$

We see that, in the Standard Model, all the quarks and charged leptons receive their masses through *Yukawa interactions* with the Higgs field. Note also that the coupling strength between the Higgs field and the fermion f is proportional to the mass of the particle.

Using expression (17), as well as

$$m_f = \frac{g_f v}{\sqrt{2}} \quad \text{and} \quad m_{\text{H}} = \sqrt{2\lambda} v \quad (24)$$

(see Eq. (4)), we obtain¹

$$v = \frac{m_{\text{W}}}{g/2} = \frac{m_{\text{H}}}{\sqrt{2\lambda}} = \frac{m_f}{g_f/\sqrt{2}} \quad (25)$$

This result is illustrated in Fig. 2 for $m_{\text{H}} = 120$ GeV.

The Higgs-fermion couplings can be extracted by measuring the **branching fractions** of the Higgs boson. There are two methods to determine the Higgs branching fractions: (1) Measure the event rate in the Higgs-strahlung process for a given final-state configuration and then divide by the total cross-section; (2) Select a sample of unbiased events in the Higgs-strahlung recoil-mass peak and determine the fraction of events that correspond to a particular decay channel. See [16] and references therein for an estimate of the accuracy that can be achieved in such measurements.

¹ We can relate v to the Fermi constant $G_{\text{F}} = 1.16639 \times 10^{-5} \text{ GeV}^{-2}$ as follows:

$$\frac{G_{\text{F}}}{\sqrt{2}} = \frac{g^2}{8m_{\text{W}}^2} = \frac{1}{2v^2} \quad \Rightarrow \quad v = (\sqrt{2} G_{\text{F}})^{-1/2} \approx 246 \text{ GeV}$$

As mentioned in Section 3, the Higgs-top coupling can be measured in the process $e^+e^- \rightarrow t\bar{t}$ at the pair-production threshold [12].

For $m_H \gtrsim 2m_W$, the **total decay width** of the Higgs boson, Γ_H , is large enough to be determined directly from the reconstructed Higgs-boson mass spectrum. The result of such an analysis is shown in [16]. For smaller Higgs-boson masses, Γ_H can be determined indirectly by employing the relation between the total and partial decay widths for a given final state:

$$\Gamma_H = \frac{\Gamma(H \rightarrow X)}{\text{BR}(H \rightarrow X)} \quad (26)$$

For instance, consider the decay $H \rightarrow WW^*$. One can directly measure the branching fraction $\text{BR}(H \rightarrow WW^*)$, determine the coupling HZZ in the process $e^+e^- \rightarrow HZ$, relate the HZZ and HWW couplings based on Eqs. (19)–(20), and then use the fact that $\Gamma(H \rightarrow WW) \propto \lambda_{HWW}^2$ to obtain the partial width $\Gamma(H \rightarrow WW^*)$ from the information on the HWW coupling. An accuracy between 4% and 15% can be achieved in the determination of Γ_H for m_H up to 160 GeV [16].

The decay modes $H \rightarrow \bar{b}b, WW$ can also be measured in photon-photon collisions with a precision similar to that expected from analyses based on e^+e^- data (see, e.g., [23]). Recall from Section 3 that the most accurate way to determine the **two-photon width** $\Gamma(H \rightarrow \gamma\gamma)$, which is sensitive to the Higgs-top coupling, is to combine data from $\gamma\gamma$ and e^+e^- collisions.

7 The proposed facility

The rich set of final states in e^+e^- and $\gamma\gamma$ collisions at a future linear collider (LC) would play an essential role in measuring the mass, spin, parity, two-photon width and trilinear self-coupling of the Higgs boson, as well as its couplings to fermions and gauge bosons; these quantities are difficult to determine with only one initial state. Furthermore, all the measurements made at LEP and SLC could be repeated using highly polarized electron beams and at much higher luminosities. For some processes within and beyond the Standard Model (e.g., the single and double Higgs-boson production), the required center-of-mass (CM) energy is considerably lower at the facility described here than at an e^+e^- or proton collider.

The proposed facility could be constructed in two stages, each with distinct physics objectives that require particular center-of-mass energies (see the preprint in [10]):

$$\text{Stage 1: } e^+e^- \rightarrow Z, WW, HZ \quad E_{ee} \sim 90 \text{ to } 250 \text{ GeV}$$

$$\text{Stage 2: } \gamma\gamma \rightarrow H, HH \quad E_{ee} \sim 160 \text{ to } 320 \text{ GeV}$$

If the e^+e^- CM energy is increased to about 340 GeV, the top-quark mass and the Higgs-top coupling could be measured in the process $e^+e^- \rightarrow t\bar{t}$; one expects $\delta m_t \approx 100 \text{ MeV} \approx 0.1\delta m_t(\text{LHC})$.

A schematic layout of an e^+e^- linear collider is shown in Fig. 10 for an X-band machine and in Fig. 14 for an L-band machine. Electron and positron beams are accelerated by a pair of linear accelerators (linacs) before colliding at an interaction point surrounded by a detector. The beams are then disposed of, and this machine cycle is repeated at a rate of 120 Hz (X-band) or 5 Hz (L-band).

The tunnels containing the main linacs should be sufficiently long to avoid relocation of the injector complexes each time an energy upgrade takes place. The production and testing of the accelerating structures and rf sources needed for such an upgrade, and the subsequent installation of the latter, can be carried out with minimal disruption to the data-taking process if the klystrons, modulators and pulse compressors are placed in a separate tunnel (see Fig. 11).

It is also envisaged that ‘bypass lines’ for low-energy beams² would be employed to accumulate data at the Z resonance in the process $e^+e^- \rightarrow Z$. This data could be used to regularly calibrate

² Bypass lines are not needed at an L-band accelerator facility.

the detector and measure the luminosity of the accelerator. Assuming a geometric luminosity $L_{e^+e^-} \approx 5 \times 10^{33} \text{ cm}^{-2} \text{ s}^{-1}$ at the Z resonance, approximately 2×10^9 Z bosons could be produced in an operational year of 10^7 s; this is about 200 times the entire LEP statistics.

8 Photon collider

The idea of using counter-directed electron linacs to create a gamma-gamma collider can be traced back to an article by P. Csonka published in 1967 [24]. The seminal work on photon colliders by I. Ginzburg et al. [25] describes in detail a method for obtaining $\gamma\gamma$ and $e\gamma$ collisions by Compton backscattering of laser light on high-energy electrons.

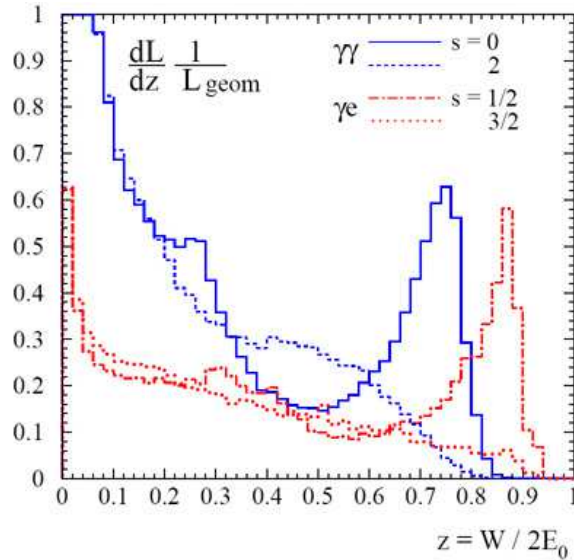


Figure 9: Simulated $\gamma\gamma$ and $e\gamma$ luminosity spectra [27] (see Section 14).

The backscattered photons have energies comparable to those of the incident electrons (see Fig. 9), and follow their direction with some small angular spread of the order of $1/\gamma$, where γ is the Lorentz factor. The spatial spread of the photons is approximately d/γ at a distance d from the Compton interaction point (CIP). Both the energy spectrum and polarization of the backscattered photons depend strongly on the polarizations of the incident electrons and laser photons. The key advantage of using e^-e^- beams at a $\gamma\gamma$ collider is that they can be polarized to a high degree.

At CIP, the electron beam is about 10 times wider than it would be at the ee collision point in the absence of a laser beam. However, since the backscattered photons follow the direction of the incident electrons, they are automatically ‘focused’ to their collision point.

The absence of beam-beam effects in $\gamma\gamma$ collisions means that it is not necessary to have very flat linac beams. The spectral luminosity of $\gamma\gamma$ collisions strongly depends on beam characteristics, but only through the parameter ρ , the ratio of the intrinsic transverse spread of the photon beam to that of the original electron beam: $\rho \equiv d/\gamma\sigma_e$. In this expression, d is the distance between CIP and the $\gamma\gamma$ collision point, and σ_e is the radius that a round Gaussian linac beam would have at the collision point in the absence of a laser beam. As ρ increases, the monochromaticity of the luminosity distribution improves (because the lowest-energy photons, which scatter at the largest angles, do not pass through the collision point), but the total luminosity decreases. For a typical photon collider, the optimal value of d is a few millimeters [26].

Assuming that the mean number of Compton interactions of an electron in a laser pulse (the Compton conversion probability) is 1, the *conversion coefficient* $k \equiv n_\gamma/n \approx 1 - e^{-1} = 0.63$,

where n_e is the number of electrons in a 'bunch' and n_γ is the number of scattered photons. The luminosity of a gamma-gamma collider is then

$$\mathcal{L}_{\gamma\gamma} = (n_\gamma/n_e)^2 \mathcal{L}_{ee} \approx (0.63)^2 \mathcal{L}_{ee} \quad (27)$$

where \mathcal{L}_{ee} is the **geometric luminosity** of electron beams:

$$\mathcal{L}_{ee} = \frac{\gamma n_e^2 N_b f}{4\pi \sqrt{\varepsilon_x \beta_x \varepsilon_y \beta_y}} \quad (28)$$

In this expression, $\varepsilon_x, \varepsilon_y$ are the *beam emittances*, β_x, β_y are the horizontal and vertical *beta functions*, respectively, N_b is the number of bunches per train, and f is the beam collision frequency. In the high-energy part of the photon spectrum, $\mathcal{L}_{\gamma\gamma} \sim 0.1 \mathcal{L}_{ee}$. However, if beams with smallest possible emittances and stronger beam focusing in the horizontal plane are used, then $\mathcal{L}_{\gamma\gamma}$ could, in principle, be made higher than $\mathcal{L}_{e^+e^-}$ [27] (see also Section 14).

9 X-band accelerator complex

A schematic layout of an X-band linear e^+e^- collider is shown in Fig. 10. The current X-band (11.4 GHz) rf technology has been developed mainly at KEK and SLAC [28]. The choice of this technology is motivated by the cost benefits of having relatively low rf energy per pulse and high accelerating gradients. The ongoing effort to develop high-gradient X-band structures is essential for the eventual construction of a CLIC-type linear accelerator [29]

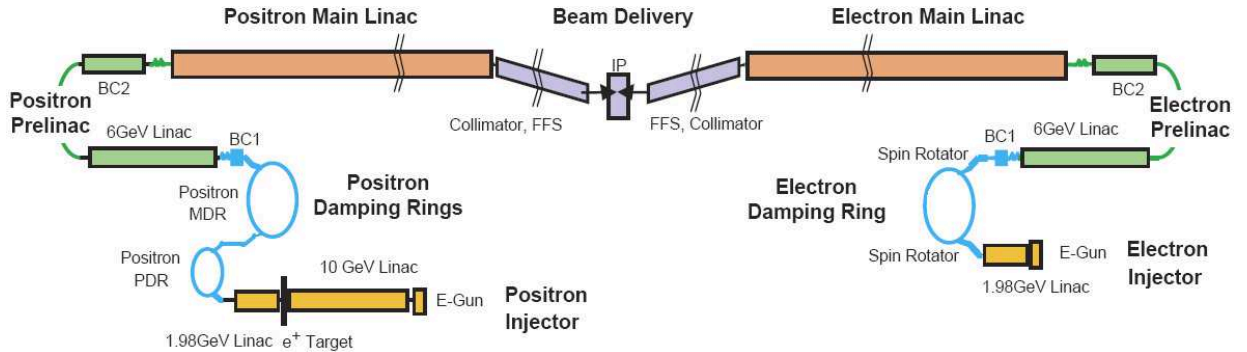


Figure 10: Schematic layout of an X-band linear e^+e^- collider [1]. With a crossing angle at the interaction point (IP), separate beam lines can be used to bring the disrupted beams to their respective dumps, thereby enabling post-IP diagnostics.

The tunnels containing the rf sources and accelerating structures are sketched in Fig. 11. A single rf unit contains a modulator that drives a pair of 60 MW klystrons, each of which generates $1.6 \mu\text{s}$ rf pulses at 120 Hz. An rf compression system enhances the peak power of the klystrons by a factor of about three, and produces 400 ns pulses that match the accelerator structure requirements.³ The resulting 380 MW, 400 ns pulses feed six 0.6 m long accelerator structures, producing a 68 (54) MV/m unloaded (loaded) gradient in each structure.

To reduce power consumption, it is proposed to use klystrons with superconducting solenoidal focusing [30]. The XL4 klystron developed at SLAC, for instance, could initially be adapted for this purpose [31].⁴

³ It takes ~ 120 ns to fill each rf cavity with an accelerating field. The remaining period of ~ 280 ns is used to accelerate a 'train' of electron bunches, which has a total length of about 270 ns.

⁴ To avoid using power-consuming solenoid electromagnets, SLAC and KEK have developed klystrons with periodic permanent magnet (PPM) focusing [31]. All PPM klystrons built so far suffer chronic rf breakdown in the output section, which manifests itself by a loss of transmitted power that develops over several hundred ns [28]. An alternative approach to the development of high-power klystrons is therefore proposed in the main text.

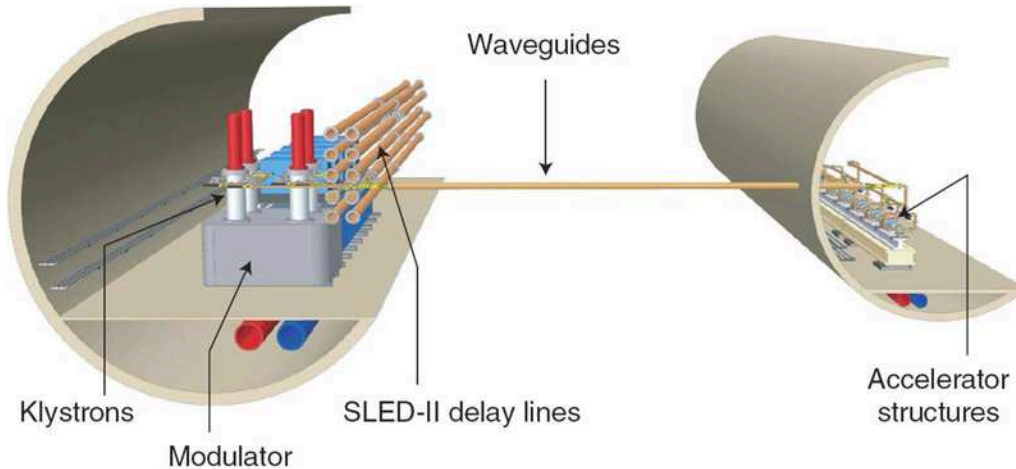


Figure 11: Dual tunnels for an X-band linear collider [1].

A comprehensive review of the status of X-band accelerator technology is given in [28]. Significant advances have been made in pulsed HV and rf power generation, high gradient acceleration and wakefield suppression. The rf sources and accelerating structures of the facility proposed here would have properties very similar to those described in [28]. The ultimate design of rf cavities, however, will depend on the outcome of the ongoing effort to develop 100 MeV/m X-band structures for a CLIC-type linear collider.

10 Laser system for an X-band machine

In order to attain maximum luminosity, every electron bunch in the accelerator should collide with a laser pulse of sufficient intensity for 63% of the electrons to undergo a Compton scattering. This requires a laser system with high average power, capable of producing pulses that would match the temporal spacing of electron bunches. The laser power is minimized when the Rayleigh range of the laser focus and the laser pulse width are matched to the electron bunch length. The proposed collider would have about 95 100-micron bunches separated by 2.8 ns, with 120 trains per second. This means that $95 \times 120 = 11,400$ laser pulses with a duration of approximately 1 ps must be produced every second. To avoid nonlinear electrodynamic effects, the maximum pulse energy should not exceed 1 joule. Therefore, the laser system ought to deliver about 11 kW of average power in pulses of a terawatt peak power, matched to the linac bunch structure.

These requirements could be satisfied, for instance, by modifying the **Mercury laser** developed at the Lawrence Livermore Lab (LLNL) for a laser fusion application, as proposed by J. Gronberg and his collaborators [32, 33] (see Fig. 12). The *Mercury laser* is designed to generate 100-J pulses with a width of 2–10 ns at a rate of 10 Hz. An initial low-energy picosecond pulse is ‘chirped’ to produce a nanosecond pulse. Once amplified in the *Mercury*, the pulse can be recombined back to the picosecond level as long as it has retained a Gaussian profile after amplification. The technique of chirped-pulse amplification, invented by D. Strickland and G. Mourou in 1985, is at the heart of all laser designs that can produce terawatt peak power. The *Mercury laser* would use Ytterbium-doped crystals (Yb:S-FAP), pumped by diode arrays, to deliver 100 J at 10 Hz with 10% efficiency for converting wall plug power to laser light. The long upper state lifetime of the crystal ($\tau = 1.26$ ms) allows the laser to be pumped more slowly, reducing the required peak diode power.

An array of 12 *Mercury lasers* can be fired sequentially to match the 120 Hz repetition rate of

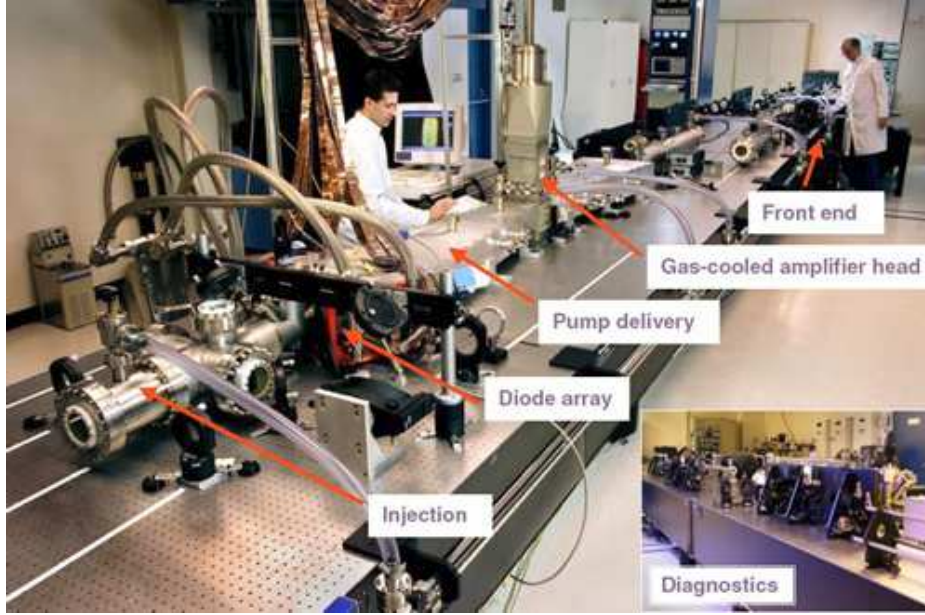


Figure 12: Photograph of the *Mercury laser*. Credit: C. Bibeau and LST.

the collider. The single 100-Joule pulse can then be subdivided and time delayed using a series of optical splitters and delay lines to produce a train of 95 1-Joule pulses separated by 2.8 ns. This would provide one laser pulse for every electron bunch in the linac. A system of focusing mirrors in the interaction region allows each laser pulse to be used twice, thus providing laser pulses for each arm of the linear accelerator.

Apart from the issue of long-term laser stability, this approach is not optimal because only one out of twelve lasers is used at a given moment, which means that a dozen independent diode arrays are required. It would be more practical if a number of special lasers with high repetition rate were used in parallel. Alternatively, one could employ an optical *free electron laser* or doped *fiber amplifiers* (see Summary).

11 Interaction region and beam dump

The **optics assembly** for the interaction region at a photon collider shown in Fig. 13 satisfies the following requirements: (a) the laser beam must be nearly co-linear with the electron beam; (b) the latter must pass through the final focusing optics; (c) the beams of electrons and laser photons must simultaneously be at the Compton interaction point; (d) the duration of the laser pulse must correspond to the electron bunch length.

The Compton scattering of laser photons on high-energy electrons results in a large energy spread in the electron beam. At the interaction point (IP), this leads to a large angular spread of the outgoing beam due to the beam-beam interaction. For nominal beam and laser parameters, the extraction beam pipe must therefore have an aperture of about ± 10 milliradians.

To remove the disrupted beams, one can use the **crab-crossing scheme** proposed by R. Palmer. In this scheme, the beams are collided at a *crossing angle* of about 10 to 20 milliradians. The same luminosity as in head-on collisions can be obtained by tilting the electron bunches with respect to the direction of the beam motion.

The aperture of the extraction beam pipe and the physical size of the final focusing magnet set a lower limit on the crossing angle of the colliding beams. The minimum crossing angle is

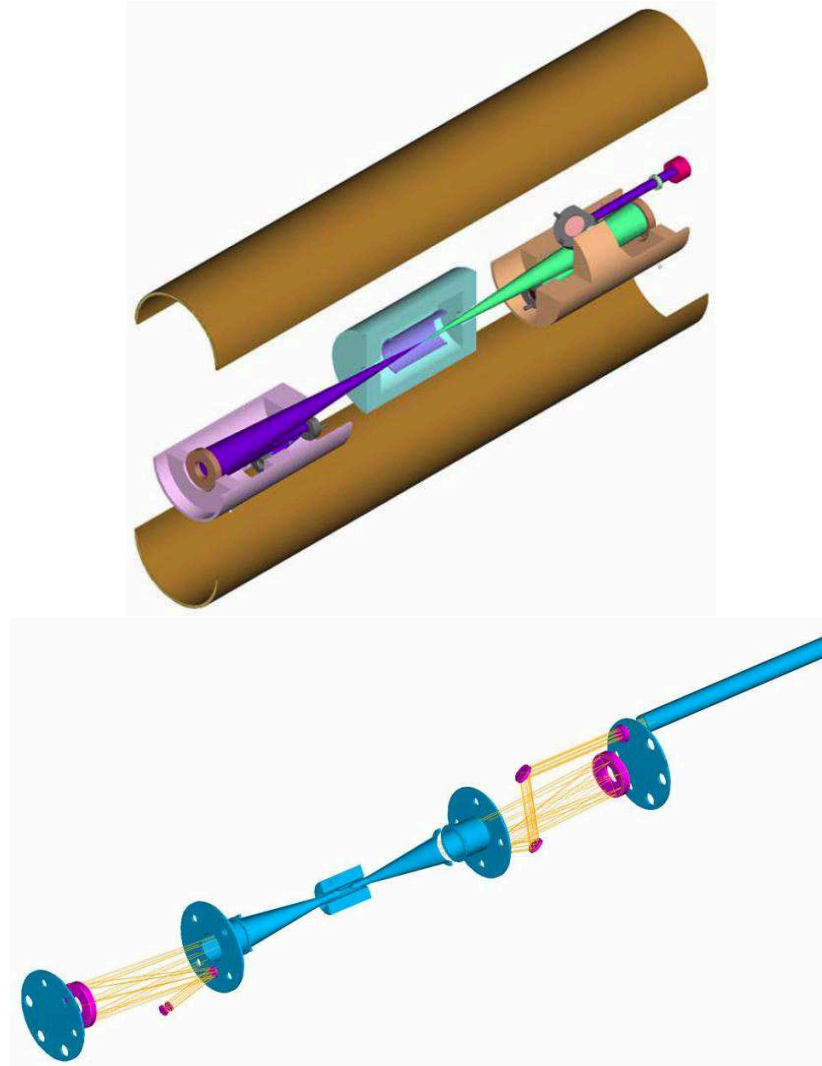


Figure 13: Optics assembly at the $\gamma\gamma$ interaction region. Electron beams and most of the background particles pass through the central hole in each of the two end-mirrors. Elements of the assembly were designed, simulated and prototyped at LLNL [34, 33].

about 25 milliradians if a final focusing quadrupole magnet with a compensating coil to minimize the fringe field is used [35].⁵ This is somewhat larger than the crossing angles envisaged for the proposed ILC and NLC e^+e^- colliders.

The ‘feedback’ system for bringing the beams into collision relies on post-IP **beam position monitors** (BPMs) that measure the beam-beam deflection at the collision point. Because of the energy spread in a highly disrupted beam, conventional BPMs may not provide sufficient resolution due to electric noise. Moreover, it is not possible to steer such a beam without large beam losses. This implies that the extraction line at a $\gamma\gamma$ collider will be a straight vacuum pipe, which precludes some post-IP diagnostics such as precise measurement of the beam energy and polarization.

Much of the extracted-beam power will be in the form of high-energy photons that have a very narrow angular spread. This would result in a large amount of energy being deposited within a small volume of the water **beam dump**, causing vaporization of H_2O . A possible solution to this problem would be to convert the photons to e^+e^- pairs in a gas target situated before the dump.

⁵ The fringe field from the final focusing magnet must be minimized to prevent low-energy particles, which are swept away by the field, from causing radiation- and heat-related problems.

In order to decrease the flux of backward-scattered neutrons, a volume filled with hydrogen or helium gas could be placed just before the gas target (see [36] and [27] for more detail).

Huge savings in construction cost could be achieved if the crossing angle and the beam dump are exactly the same for the operation of the accelerator in the e^+e^- and $\gamma\gamma$ collision modes. The beam dump described in [36] is designed with this in mind. The part of the extraction line containing a chicane — which provides vertical displacement and dispersion needed for continuous measurements of the beam energy spectrum and polarization at an e^+e^- collider — could be replaced with a straight vacuum pipe for the operation in the $\gamma\gamma$ mode.

12 L-band (TESLA-type) accelerator complex

A detailed description of the current design for the *International Linear Collider* (ILC) can be found in [37] (see Fig. 14). This design, based on the superconducting technology originally developed at DESY, uses L-band (1.3 GHz) rf cavities that have average accelerating gradients of 31.5 MeV/m. A single superconducting niobium cavity is about 1 m long. Nine cavities are mounted together in a string and assembled into a common low-temperature cryostat or *cryomodule* (see Fig. 15), which is 12.652 m long.⁶

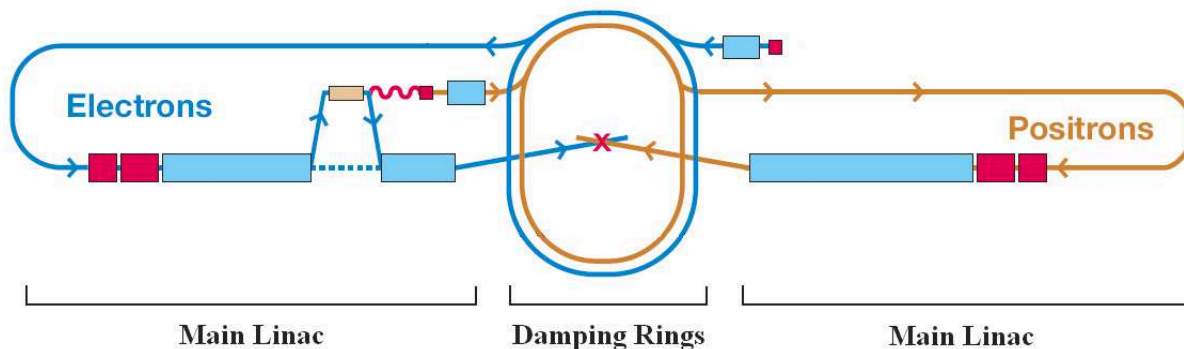


Figure 14: Schematic layout of an L-band (TESLA-type) linear collider; credit: ILC collaboration. Each linac consists of a few thousand superconducting cavities placed within cryogenic vessels to form cryomodules (see Fig. 15). Liquid helium is used to cool cavities to -271°C .

The ILC main linacs are composed of rf units, each of which is formed by three contiguous cryomodules containing 26 nine-cell cavities. Every unit has an rf source, which includes a pulse modulator, a 10 MW multi-beam klystron, and a waveguide system that distributes the power to the cavities.

A TESLA-type design offers some advantages over the X-band technology:

- Wakefields are drastically reduced due to the large size of the rf cavities, which means that cavity alignment tolerances can be relaxed;
- Superconducting rf cavities can be loaded using a long rf pulse (1.5 ms) from a source with low peak rf power;
- ‘Wall-plug to beam’ power transfer efficiency is about twice that of X-band cavities;
- The long rf pulse allows a long bunch train (~ 1 ms), with many bunches (~ 2600) and a relatively large bunch spacing (~ 370 ns). A trajectory correction (feedback) system within the train can therefore be used to bring the beams into collision.

⁶ A 20-GeV linac containing 116 cryomodules is currently under construction at DESY. This facility will serve both as an X-ray free electron laser (XFEL) and an important testbed for the ILC.

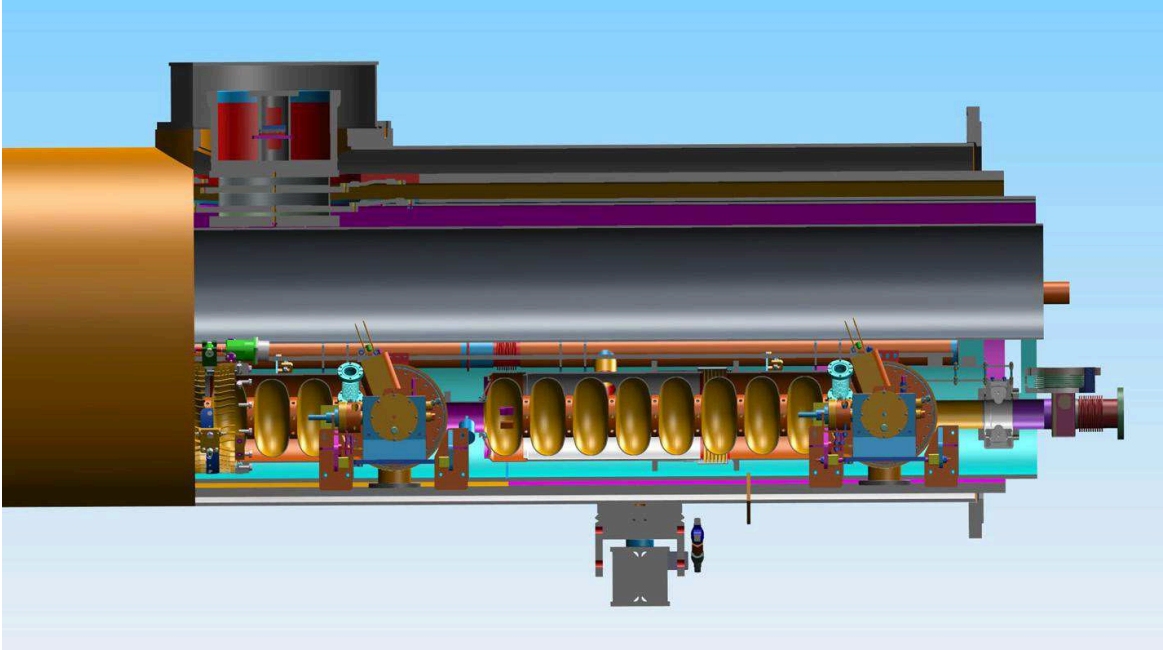


Figure 15: An inside view of a cryomodule for the ILC. Credit: Fermilab.

However, in contrast to a compact, high-gradient X-band machine, a collider based on the current TESLA-type design would be characterized by low accelerating gradients ($\lesssim 30$ MeV/m), damping rings that a few kilometers in circumference, and a technologically challenging cryogenic system (see Fig. 15) that requires a number of surface cryogenic plants.

If the initial operation of the proposed facility is in the $\gamma\gamma$ mode, there would be no need for an e^+ source. Two electron damping rings could then be built inside a single tunnel. For operation at the nominal e^+e^- luminosity, a positron damping ring would later replace one of the electron rings. In any case, the present design of the positron source (see Fig. 14) should be greatly simplified.

13 Laser system for an L-band machine

To use *Mercury lasers* with a TESLA-type machine, which has a bunch structure very different from that of an X-band collider, would require prohibitively large average power and development of special electro-optical switches. Alternatively, one could take advantage of the large inter-bunch spacing in the TESLA-type linac and use a ~ 100 -m long optical cavity that would allow a single laser pulse to travel around a ring, colliding with all the bunches. However, it is extremely difficult to achieve required precision in the construction of such a cavity. A particularly undesirable feature of this scheme is a large ‘dead angle’ (± 95 mrad) for particle tracking inside the detector [27].

A possible source of primary photons for a $\gamma\gamma$ collider is an optical *free electron laser* (FEL). The radiation produced by an FEL has a variable wavelength, and is fully polarized either circularly or linearly depending on whether the undulator is helical or planar, respectively. The required time structure of laser pulses can be achieved by using a modified design of the main linac as a driving accelerator for the FEL. A free electron laser for the photon collider at a TESLA-type machine is described in [38].

14 Luminosity and backgrounds at a $\gamma\gamma$ collider

Since the cross-sections $\sigma_{\gamma\gamma \rightarrow \text{HH}}$ and $\sigma_{e^+e^- \rightarrow \text{HHZ}}$ do not exceed 0.4 fb, it is essential to attain the highest possible luminosity, rather than energy, in order to measure the trilinear Higgs self-coupling. If beams with smallest possible emittances and stronger beam focusing in the horizontal plane are used, then the $\gamma\gamma$ luminosity $\mathcal{L}_{\gamma\gamma}$ could, in principle, be made higher than $\mathcal{L}_{e^+e^-}$, as explained in what follows [27].

Assuming the ‘nominal’ ILC beam parameters for the operation of the accelerator in the e^+e^- mode [37],⁷ the expected $\gamma\gamma$ luminosity in the high-energy part of the photon spectrum

$$\mathcal{L}_{\gamma\gamma}(\text{high-energy peak}) \sim 3.5 \times 10^{33} \text{ cm}^{-2} \text{ s}^{-1} \sim 0.2 \mathcal{L}_{e^+e^-}$$

where $\mathcal{L}_{e^+e^-} = 2 \times 10^{34} \text{ cm}^{-2} \text{ s}^{-1}$ is limited by collision effects (beamstrahlung and beam instabilities). At a photon collider with center-of-mass energies $\lesssim 500$ GeV, and for electron beams that are not too short, coherent pair production is suppressed due to the broadening and displacement of the electron beams during their collision [26]. In this case, $\mathcal{L}_{\gamma\gamma}$ is limited *only* by the transverse area of the beam (note that its vertical size is much smaller than the horizontal):

$$\mathcal{L}_{\gamma\gamma} \propto (\sigma_x \sigma_y)^{-1} \quad \sigma_{x,y} = \sqrt{\beta_{x,y}(\varepsilon_{x,y}/\gamma)} \quad (29)$$

as can be seen from expressions (27) and (28) in Section 8.

The beam emittances in Eq. (29) are determined by various physics effects inside a damping ring (see Fig. 16). If the synchrotron radiation is dominated by the ring’s wiggler parameters (large F_w), and if the quantum excitation by the wiggler is not too large compared with that in the arcs, then from Eqs. (33) and (14) in [39] it follows that the horizontal beam emittance ε_x could be significantly reduced by using a wiggler with short period and a judiciously chosen value of the peak field (in order to preserve the damping time). The vertical emittance ε_y is *not* determined by the wiggler, but by optics errors that are not easily characterized. Assuming that both ε_x and ε_y could be reduced by about a factor of five compared with their ‘nominal’ ILC values, $\mathcal{L}_{\gamma\gamma}$ would then exceed $\mathcal{L}_{e^+e^-}$:

$$\mathcal{L}_{\gamma\gamma}(\text{high-energy peak}) \sim 2.5 \times 10^{34} \text{ cm}^{-2} \text{ s}^{-1} \sim 1.2 \mathcal{L}_{e^+e^-}$$

To obtain this result it was also assumed that $\beta_x = 1.7$ mm, and that the distance between the interaction and conversion regions is 1 mm. Simulated luminosity spectra for these parameters are shown in Fig. 9.

At a $\gamma\gamma$ collider, the spectrum of photons after Compton scattering is broad, with a characteristic peak at maximum energies (see Fig. 9). The low-energy part of the spectrum is produced by multiple Compton scattering of electrons on photons inside laser beams.

The Compton-scattered photons can have circular or linear polarizations, depending on their energies and the polarizations of the initial electrons and laser light. For instance, the scattered photons have an average helicity $\langle \lambda_\gamma \rangle \neq 0$ if either the laser light has a circular polarization $P_c \neq 0$ or the incident electrons have a mean helicity $\langle \lambda_e \rangle \neq 0$. In the case $2P_c \lambda_e = -1$, which results in a good monochromaticity of the backscattered photon beam, the average degree of circular polarization of the photons within the high-energy peak of the luminosity distribution is over 90%.

Since the polarization of Compton-scattered photons depends strongly on their energy, the **luminosity spectrum** has to be measured separately for different polarization states. When both photons are *circularly polarized*, the process $\gamma\gamma \rightarrow e^+e^-, \mu^+\mu^-$ is particularly well suited for measuring the spectral luminosity [40]. This process has a cross-section of a few pb for a total $\gamma\gamma$ angular momentum $|J_z| = 2$. A precision of about 0.1% is expected in one year of running, which

⁷ The ‘nominal’ ILC beam parameters are: $N_b = 2 \times 10^{10}$, $\sigma_z = 0.3$ mm, $f = 14100$ Hz, $\varepsilon_x = 10^{-5}$ m and $\varepsilon_y = 4 \times 10^{-8}$ m. While it is feasible to obtain $\beta_y \sim \sigma_z = 0.3$ mm, the minimum value of β_x is restricted, by chromo-geometric aberrations in the final-focus system and for the above horizontal emittance, to about 5 mm.



Figure 16: Arc section of the ATF Damping Ring, which produces the world’s smallest-emittance beams. The layout of the magnets in the arc sections is designed to achieve small equilibrium emittances. The wiggler magnets in the straight sections of the ring shorten the damping time. Fast kicker magnets and DC septum magnets are used for beam extraction. Credit: KEK.

is better than the accuracy needed for the Higgs-boson studies described in this note. To measure the luminosity spectrum in the $|J_z| = 0$ configuration, the helicity of one of the photon beams can be inverted by simultaneously changing the signs of the helicities of both the laser and electron beams. For the product of photon *linear polarizations*, the spectral luminosity can be measured in the above process by studying the azimuthal variation of the cross-section at large angles [40, 26].

Undisrupted electron beams at a $\gamma\gamma$ collider can be steered using a fast feedback system that measures their deflection (see Section 11). Once the electron beams are brought into collision, the laser will be turned on. The scattered photons follow the direction of the incident electrons.

Multiple Compton scattering of electrons on photons leads to a low-energy ‘tail’ in the energy spectrum of the electrons. At the interaction point, this results in a large deflection angle of the e^-e^- beams. Due to a finite crossing angle (see Section 11), the outgoing beams are also deflected vertically by the solenoidal magnetic field of the detector. Fig. 19 in [41] shows the angular spread of an outgoing electron beam right after the interaction point and at $z = 2.8$ m. The problem of ‘stabilizing’ beam-beam collisions, and hence the $\gamma\gamma$ luminosity, is discussed in [27].

The **backgrounds** at a photon collider caused by beam-beam effects in the interaction region have been simulated considering both the *incoherent* particle-particle and *coherent* particle-beam electromagnetic (QED) interactions described in [26]. Another significant source of background is due to backscattering of particles. The hadronic structure of the photon arises from the possibility that it can either split into a quark-antiquark pair or transform into a vector meson, with the probability of about 1/200. At the expected ILC $\gamma\gamma$ luminosity, for instance, the average number of hadronic background events per one bunch collision is about two [26]. The above backgrounds influence data acquisition and analysis, as well as the operation of various detector components, as discussed in [26, 41].

15 Summary and Acknowledgements

The rich set of final states in e^+e^- and $\gamma\gamma$ collisions at a future linear collider would play an essential role in measuring the mass, spin, parity, two-photon width and trilinear self-coupling of the Higgs boson, as well as its couplings to fermions and gauge bosons (see Sections 3 to 6); these quantities are difficult to determine with only one initial state. For some processes within and beyond the Standard Model, the required center-of-mass energy is considerably lower at the facility described here than at an e^+e^- or proton collider.

Since the cross-sections $\sigma_{\gamma\gamma \rightarrow \text{HH}}$ and $\sigma_{e^+e^- \rightarrow \text{HHZ}}$ do not exceed 0.4 fb, it is essential to attain the highest possible luminosity, rather than energy, in order to measure the trilinear Higgs self-coupling. If beams with smallest possible emittances and stronger beam focusing in the horizontal plane are used, then the luminosity $\mathcal{L}_{\gamma\gamma}$ could be made higher than $\mathcal{L}_{e^+e^-}$ (see Section 14).



Figure 17: The 8-GeV electron linac (left) and the in-vacuum undulator of the X-ray free electron laser (XFEL) at the SPring-8 facility in Japan [42]. The C-band rf system of the linac can produce an accelerating gradient of 32 MV/m using 50 MW klystrons.

The proposed $e^+e^-/\gamma\gamma$ collider would be constructed in three stages, each with a distinct physics objective that requires a particular center-of-mass energy (see Section 7 and the preprint in [10]). Together with LHC, such a facility would bridge the gap between the present high-energy frontier and that accessible to a TeV-scale e^+e^- or muon collider.

An L-band (TESLA-type) linear collider offers some advantages over an X-band machine (see Section 12). However, in contrast to a compact, high-gradient X-band accelerator, a collider based on the current TESLA-type design would be characterized by low accelerating gradients ($\lesssim 30$ MeV/m), damping rings that are a few kilometers in circumference, and a technologically challenging cryogenic system that requires a number of surface cryogenic plants. One should also bear in mind that the ongoing effort to develop 100 MeV/m X-band accelerating structures is essential for the eventual construction of a TeV-scale linear collider based on the CLIC design.

If the initial operation of the proposed facility is in the $\gamma\gamma$ mode, there would be no need for an e^+ source. Two electron damping rings could then be built inside a single tunnel in the case of a TESLA-type machine. For operation at the nominal e^+e^- luminosity, a positron damping ring would later replace one of the electron rings.

A possible source of primary photons for a $\gamma\gamma$ collider is: an optical *free electron laser* (FEL), diode-pumped *solid state lasers*, or doped *fiber amplifiers* (see Sections 10 and 13). The radiation produced by an FEL has a variable wavelength, and is fully polarized either circularly or linearly. Each of the X-ray free electron lasers (XFELs) currently under development at SLAC (S-band), DESY (L-band) and the SPring-8 facility (C-band; see Fig. 17) can serve as a testbed for both an

optical FEL and the main linac of a future linear collider.⁸ An optical FEL could be placed in a separate tunnel connected to the experimental hall housing the detector.

Elements of the optics assembly for the interaction region at a photon collider were designed, simulated and prototyped at LLNL (see Section 11). The Compton scattering of laser photons on high-energy electrons results in a large energy spread in the electron beam. At the interaction point, this leads to a large angular spread of the outgoing beam due to the beam-beam interaction. To remove the disrupted beams, one can use the crab-crossing scheme described in Section 11. Huge savings in construction cost could be achieved if the crossing angle and the beam dump are exactly the same for the operation of the accelerator in the e^+e^- and $\gamma\gamma$ collision modes.

Acknowledgements

I am grateful to K. Flöttmann, K. Fujii, S. Fukuda, J. Gronberg, K. Hagiwara, T. Higo, S. Hiramatsu, G. Jikia, S. Kazakov, S. Matsumoto, A. Miyamoto, Y. Okada, A. Seryi, D. Sprehn, N. Toge, A. Wolski and K. Yokoya for many useful discussions regarding various aspects of this proposal.

References

- [1] GLC Project Report, K. Abe et al. (2003).
- [2] The LEP Collaborations, R. Barate et al., Phys. Lett. B **565**, 61 (2003).
- [3] J. Erler et al., Phys. Lett. B **486**, 125 (2000).
- [4] H. E. Haber and R. Hempfling, Phys. Rev. Lett. **66**, 1815 (1991); Y. Okada, M. Yamaguchi and T. Yanagida, Prog. Theor. Phys. **85**, 1 (1991); J. R. Ellis, G. Ridolfi and F. Zwirner, Phys. Lett. B **257**, 83 (1991).
- [5] M. Carena et al., Phys. Lett. B **355**, 209 (1995); M. Carena, M. Quiros and C. Wagner, Nucl. Phys. B **461**, 407 (1996); H. E. Haber, R. Hempfling and A. Hoang, Z. Phys. C **75**, 539 (1997); S. Heinemeyer, W. Hollik and G. Weiglein, Eur. Phys. J. C **9**, 343 (1999); G. Degrassi et al., Eur. Phys. J. C **28**, 133 (2003).
- [6] J. J. van der Bij, Nucl. Phys. B **267** (1986) 557.
- [7] E. Boos et al., Nucl. Inst. Meth. A **472**, 100 (2001).
- [8] R. Belusevic, *Low-Energy Photon Collider*, KEK Preprint 2003-2 (2003).
- [9] M. Mühlleitner et al., DESY 00-192; hep-ph/0101083 (2001).
- [10] R. Belusevic and G. Jikia, Phys. Rev. D **70**, 073017 (2004); hep-ph/0403303.
- [11] U. Baur, T. Plehn and D.L. Rainwater, Phys. Rev. D **68**, 033001 (2003).
- [12] K. Fujii, T. Matsui and Y. Sumino, Phys. Rev. D **50**, 4341 (1994).

⁸ The wavelength λ of FEL radiation is determined by $\lambda \approx \lambda_u/2\gamma^2$, where γ is the Lorentz factor of the electron beam and λ_u is the periodic length of the undulator. Although an optical FEL requires a much smaller electron linac and a considerably simpler undulator than an XFEL, the charge per electron beam bunch has to be sufficiently large (~ 4 nC) to produce photon pulses of ~ 1 J. Suitable high-intensity and low-emittance rf guns have already been developed [43].

- [13] B. Grzadkowski and J. Gunion, Phys. Lett. B **294**, 361 (1992).
- [14] K. Hagiwara, Nucl. Instrum. Meth. A **472**, 12 (2001).
- [15] K. Abe et al., GLD Detector Outline Document (2006).
- [16] S. Heinemeyer et al., CERN-PH-TH/2005-228; hep-ph/0511332.
- [17] A. Djouadi et al., Eur. Phys. J. C **10**, 27 (1999).
- [18] D. J. Miller and S. Moretti, Eur. Phys. J. C **13**, 459 (2000).
- [19] C. Castanier et al., hep-ex/0101028.
- [20] G. Belanger et al., Phys. Lett. B **576**, 152 (2003).
- [21] G. Jikia, Nucl. Phys. B **412**, 57 (1994).
- [22] I. Ginzburg et al., Nucl. Instrum. Meth. **219**, 5 (1984).
- [23] D. Asner et al., Eur. Phys. Journal C **28**, 27 (2003).
- [24] P. Csonka, Phys. Lett. B **24**, 625 (1967); CERN Yellow Report TH 772 (1967).
- [25] I. Ginzburg et al., Nucl. Instrum. Meth. **205**, 47 (1983).
- [26] B. Badalek et al., Int. J. Mod. Phys. **19**, 5097 (2004).
- [27] V. Telnov, Acta Phys. Pol. B **37**, 1049 (2006).
- [28] C. Adolphsen, *Advances in Normal Conducting Accelerator Technology from the X-band Linear Collider Program*, SLAC-PUB-11224, and Proceedings PAC-2005.
- [29] J. Ellis and I. Wilson, Nature **409**, 431–435 (18 January 2001).
- [30] T. Ogitsu et al., SLAC-REPRINT-1995-015 (1995).
- [31] D. Sprehn et al., SLAC-PUB-11162 (2004).
- [32] J. Gronberg et al., Proc. 2001 Part. Accel. Conf., Chicago.
- [33] J. Gronberg, ALC Workshop, SLAC (2004).
- [34] K. Skulina et al., *The Future of Particle Physics*, Snowmass Conf. 2001.
- [35] B. Parker et al., Proc. 2007 Part. Accel. Conf., Albuquerque; SLAC-PUB-12832 (2007).
- [36] L. Shekhtman and V. Telnov, physics/0411253.
- [37] ILC Reference Design Report, G. Aarons et al. (2007).
- [38] E. Saldin, E. Schneidmiller and M. Yurkov, Nucl. Instrum. Meth. A **472**, 94 (2001).
- [39] P. Emma and T. Raubenheimer, Phys. Rev. STAB, Vol. **4**, 021001 (2001).
- [40] A. Pak et al., BUDKER-INP 2003-7; hep-ex/0301037.
- [41] F. Bechtel et al., Nucl. Instrum. Meth. A **564**, 243 (2006).
- [42] SCSS X-FEL Conceptual Design Report, May 2005.
- [43] P. Michelato, Proc. EPAC08, Genoa (2008); K. Flöttmann, private communication.